Materials Research Proceedings 41 (2024) 457-466 https://doi.org/10.21741/9781644903131-51

Considering the viscoelastic material behavior in a solid-shell element for thermoforming simulation

MITSCH Johannes[1,a *], SCHÄFER Bastian[1,b], WANK Jan Paul[1,c] and KÄRGER Luise[1,d]

[1]Karlsruhe Institute of Technology (KIT), Institute of Vehicle System Technology (FAST) – Lightweight Engineering, 76131 Karlsruhe Germany

[a] Johannes.Mitsch@kit.edu

Keywords: Solid-Shell, Thermoforming, Process Simulation, Finite Element-Analysis

Abstract. To predict manufacturing effects in the thermoforming process for fiber reinforced plastics the Finite Element Method is widely used. Most macroscopic simulation methods are based on conventional two-dimensional shell elements which are not capable of modeling the material behavior in thickness direction using constitutive equations. At the same time, standard three-dimensional element formulations are not suitable for the forming simulation of thin textiles due to numerical locking phenomena and the lack of a possible membrane-bending-decoupling. Previous studies focused on a specialized solid-shell element formulation which provides anisotropic but purely elastic material modeling. Since purely elastic approaches cannot accurately describe the deformation behavior in the thermoforming process, the provided element formulation is enhanced to rate-dependent viscoelastic material modeling. Numerical studies are carried out that reveal that the membrane-bending-decoupling is preserved for the viscoelastic material model. Virtual coupon tests demonstrate the rate-dependent material behavior in the solid-shell element. The obtained results show that the general approach of the viscoelastic material behavior within the solid-shell element is suitable to address out-of-plane phenomena in thermoforming simulations.

Introduction

Fiber reinforced plastics (FRPs) like thermoplastic tapes provide great lightweight potential due to their high mass specific stiffness and strength while also having the possibility to be tailored for specific applications [1]. Precise computer-aided component design is the key to component concepts with reliable high load-bearing capacity combined with low masses.

Most macroscopic simulations of the forming process of thermoplastic tapes are based on conventional shell elements [2]. Since FRP components are usually thin, conventional shells provide efficient simulation of the in-plane membrane and out-of-plane bending behavior. However, the material modeling in thickness direction is not possible since conventional shells are only two-dimensional. To enable material modeling in thickness direction three-dimensional element types must be used. Standard three-dimensional element formulations are not suitable for the forming simulation of thin textiles due to numerical locking phenomena and the lack of a possible membrane-bending-decoupling [3]. Therefore, specialized element formulations, like solid-shell elements are required.

The focus of this work is the simulation of the thermoforming process of preimpregnated textile composites, e.g., thermoplastic tapes. Due to the influence of the matrix, the material behavior, and the bending behavior of preimpregnated FRPs is rate- and temperature-dependent. Hence, (thermo-)viscoelastic material modeling is crucial for the proper simulation of the thermoforming process of preimpregnated textile composites. Thus, purely elastic approaches are unsuitable for modeling the material behavior in forming simulation of thermoplastic composites [4–6]. Dörr et al. [7,8] use a Voigt-Kelvin and a generalized Maxwell approach to model the isothermal

viscoelastic material behavior. Subsequently, this approach was further developed to a thermoviscoelastic material law [9].

In context of the forming simulation for thermoplastic composite prepregs, Xiong [10] and Xiong et al. [11] present a prismatic solid-shell element to display consolidation and compaction. The approach is based on a DKT plate element with an additional degree of freedom in the middle of the element. A viscoelastic material law based on a generalized Maxwell model is utilized to model both the in-plane shear behavior and the compaction behavior. Another approach to display non-elastic material properties in thickness direction of preimpregnated textile composites is presented by Mulye et al. [12]. A so-called pinching shell element is introduced which is based on a shell element. In their work an elasto-plastic material model is chosen

The 3D hexahedral solid-shell element considered in the present study continues the investigations by Schäfer et al. [3,13]. Initially based on the work of Schwarz and Reese [14,15] who proposed a solid-shell element with only translational degrees of freedom for isotropic material laws, Pagani et al. [16] extended the formulation to the explicit case. Schäfer et al. [3,13] enhanced the element formulation for anisotropic elastic material laws. An approach for a membrane-bending-decoupling, which is based on a Taylor series approximation of the strain, is also presented. The considered solid-shell element is implemented by means of a user-element (VUEL) for the FEM solver ABAQUS/EXPLICIT. The implementation of the user-element is done using the MATHEMATICA-based programming environment ACEGEN [17] which allows symbolic implementation and differentiation in combination with runtime optimization.

In this work the solid-shell element is extended to viscoelastic material behavior. For this, the Voigt-Kelvin model is implemented and evaluated separately for the membrane and the bending part. To evaluate the viscoelastic material law, the deformation gradient $\boldsymbol{F}$ is needed to derive the deformation rate tensor $\boldsymbol{D}$ from the rate of the Green-Lagrange strain tensor $\boldsymbol{E}$. Since the Green-Lagrange strain tensor $\boldsymbol{E}$ is modified using the enhanced assumed strain- (EAS) and the assumed natural strain- (ANS) method, the corresponding deformation gradient $\boldsymbol{F}$ cannot solely be described by the node displacements within the element. Hence, an alternative method to calculate an effective deformation gradient $\boldsymbol{F}_{\mathrm{tec}}$ is presented. An alternative approach to ensure numerical stability is considered. It is shown that the decomposition of the membrane- and bending-behavior still holds. Numerical studies are carried out to demonstrate the rate-dependency of the implemented viscoelastic material behavior for both the membrane and the bending behavior.

Solid-Shell Element

Solid-shell formulation. The 3D hexahedral solid-shell element considered in the present study is based on the work of Schäfer et al. [3,13]. Its eight nodes have only translational degrees of freedom. It is implemented as a user-element (VUEL) in ABAQUS/EXPLICIT. A reduced integration scheme is used for the in-plane deformations. Thus, there is only one single integration point in the center of the shell plane. Along the thickness direction of the element, multiple integration points are located to account for the material behavior in the out-of-plane direction. Analogously to Schäfer et al. [3,13], the total Green-Lagrange strain tensor $\boldsymbol{E}$ is modified using the EAS- and the ANS-concept. The EAS-concept introduced by Simo et al. [18–20] helps to prevent volumetric and Poisson thickness locking by introducing an enhanced strain $\boldsymbol{E}_{\mathrm{e}}$. It is added to the compatible strain $\boldsymbol{E}_{\mathrm{c}}$ for the total strain $\boldsymbol{E} = \boldsymbol{E}_{\mathrm{c}} + \boldsymbol{E}_{\mathrm{e}}$. The compatible part $\boldsymbol{E}_{\mathrm{c}}$ is solely dependent on the displacements $\boldsymbol{u}_i$ of the eight nodes within the element. The ANS-method introduced by Hughes and Tezduya [21] helps to prevent transverse shear and curvature thickness locking. More comprehensive explanations on the ANS- and EAS-concepts are given by [14,15,22]. In the following, $\boldsymbol{E}_{\mathrm{mod}}$ denotes the modified strain using the EAS- and ANS-method.

Using a Taylor expansion for the compatible strain $\boldsymbol{E}_{\mathrm{c}}$ with respect to the element-center enables the decomposition of the total strain $\boldsymbol{E}_{\mathrm{mod}}$ into (cf. [13–15])

Materials Research Proceedings 41 (2024) 457-466 https://doi.org/10.21741/9781644903131-51

$$\boldsymbol{E}_{\mathrm{mod}} = \underbrace{\boldsymbol{E}_{\mathrm{c}}^{0}}_{\boldsymbol{E}_{\mathrm{M}}} + \underbrace{\zeta \boldsymbol{E}_{\mathrm{c}}^{\zeta} + \zeta^{2} \boldsymbol{E}_{\mathrm{c}}^{\zeta\zeta} + \boldsymbol{E}_{\mathrm{e}}}_{\boldsymbol{E}_{\mathrm{B}}} + \boldsymbol{E}_{\mathrm{c}}^{\mathrm{hg}}. \tag{1}$$

Here, $\boldsymbol{E}_{\mathrm{c}}^{0}$ is the compatible strain in the element-center which is used as the membrane strain $\boldsymbol{E}_{\mathrm{M}}$. The tensors $\boldsymbol{E}_{\mathrm{c}}^{\zeta}$ and $\boldsymbol{E}_{\mathrm{c}}^{\zeta\zeta}$ denote the first and second derivatives of $\boldsymbol{E}_{\mathrm{c}}$ with respect to the isoparametric thickness coordinate ζ. They are used with the enhanced strain $\boldsymbol{E}_{\mathrm{e}}$ as the bending strain $\boldsymbol{E}_{\mathrm{B}}$. The remaining parts of the Taylor expansion $\boldsymbol{E}_{\mathrm{c}}^{\mathrm{hg}}$ describe the in-plane deformation and are used to prevent hourglass deformation.

Analogously, the stress $\boldsymbol{S}$ can be split into (cf. [13–15])

$$\boldsymbol{S} = \boldsymbol{S}_{\mathrm{M}}^{*}(\boldsymbol{E}_{\mathrm{M}}) + \boldsymbol{S}_{\mathrm{B}}^{*}(\boldsymbol{E}_{\mathrm{B}}) + \boldsymbol{S}^{\mathrm{hg}}\left(\boldsymbol{E}_{\mathrm{c}}^{\mathrm{hg}}\right). \tag{2}$$

The stresses $\boldsymbol{S}_{\mathrm{M}}^{*}$ and $\boldsymbol{S}_{\mathrm{B}}^{*}$ describe the membrane and the bending stresses that are related to the out-of-plane integration. The hourglass stress $\boldsymbol{S}^{\mathrm{hg}}$ solely depends on $\boldsymbol{E}_{\mathrm{c}}^{\mathrm{hg}}$ and is used for the hourglass stabilization. The combination of Eq. 1 and Eq. 2 enables the membrane-bending decoupling within the solid-shell element. All stresses in Eq. 2 are modeled purely elastic by Schäfer et al [13].

Viscoelastic material law. To model the rate-dependency, the Voigt-Kelvin approach is considered. It is based on the parallel connection of the elastic part with a viscous part. Thus, the second Piola-Kirchhoff stress $\boldsymbol{S}$ using the Voigt-Kelvin model is calculated by [23]

$$\boldsymbol{S} = \boldsymbol{S}_{\mathrm{elast}} + \boldsymbol{S}_{\mathrm{visc}}. \tag{3}$$

The elastic part $\boldsymbol{S}_{\mathrm{elast}}$ is evaluated using the hyperelastic St. Venant-Kirchhoff model [24]

$$\boldsymbol{S}_{\mathrm{elast}} = \mathbb{C}[\boldsymbol{E}]. \tag{4}$$

Here $\mathbb{C}$ is the stiffness tensor and $\boldsymbol{E}$ the Green-Lagrange strain. To evaluate the viscous part $\boldsymbol{S}_{\mathrm{visc}}$, the isotropic Newton model is used. The viscous law is given by [25]

$$\boldsymbol{\sigma}_{\mathrm{visc}} = 2\eta \boldsymbol{D}. \tag{5}$$

Here η is the viscosity, $\boldsymbol{D}$ the symmetric part of the velocity gradient, respectively the deformation rate tensor, and $\boldsymbol{\sigma}_{\mathrm{visc}}$ the resulting Cauchy stress. The deformation rate tensor $\boldsymbol{D}$ can be calculated dependent on $\dot{\boldsymbol{E}}$ using [23]

$$\boldsymbol{D} = \boldsymbol{F}^{-\mathsf{T}} \dot{\boldsymbol{E}} \boldsymbol{F}^{\mathsf{T}}. \tag{6}$$

To apply Eqs. 3 to 6 on the solid-shell element, the Green-Lagrange strain tensor $\boldsymbol{E}$ is used for the elastic part (Eq. 3) and the rate $\dot{\boldsymbol{E}}$ for the viscous part (Eq. 5 and Eq. 6). In Eq. 6 the deformation gradient $\boldsymbol{F}$ is required to obtain $\boldsymbol{D}$. However, within the solid-shell element the total Green-Lagrange strain tensor is modified using the EAS- and the ANS-method. Consequently, the deformation gradient $\boldsymbol{F}$ that is derived solely from the nodal displacements $\boldsymbol{u}_i$ does not necessarily describe the same deformation state as $\boldsymbol{E}_{\mathrm{mod}}$. Due to the symmetry of strain tensors, it is impossible to derive $\boldsymbol{F}$ directly from $\boldsymbol{E}$. Thus, a suitable approximation $\boldsymbol{F}_{\mathrm{tec}}$ for $\boldsymbol{F}$ in dependency of $\boldsymbol{E}_{\mathrm{M}}$, respectively $\boldsymbol{E}_{\mathrm{B}}$, has to be defined to evaluate Eq. 6. Hauptmann et al. [26] presented a procedure to calculate a deformation gradient $\boldsymbol{F}_{\mathrm{tec}}$ from a modified Green-Lagrange strain tensor $\boldsymbol{E}_{\mathrm{tec}}$ which is adopted in this work. For this, the polar decomposition of $\boldsymbol{F}_{\mathrm{tec}}$ is performed

Materials Research Proceedings 41 (2024) 457-466 https://doi.org/10.21741/9781644903131-51

$$\boldsymbol{F}_{\mathrm{tec}} = \boldsymbol{R}\boldsymbol{U}_{\mathrm{tec}}. \tag{7}$$

The stretch tensor $\boldsymbol{U}_{\mathrm{tec}}$ is a symmetric second-order tensor. It can be derived from $\boldsymbol{E}_{\mathrm{tec}}$ using

$$(\boldsymbol{U}_{\mathrm{tec}})^2 = 2\boldsymbol{E}_{\mathrm{tec}} + \boldsymbol{I}. \tag{8}$$

Here, $\boldsymbol{I}$ is the identity for second-order tensors. The tensor $\boldsymbol{R}$ in Eq. 7 is an orthogonal second-order tensor. It cannot be obtained from $\boldsymbol{E}_{\mathrm{tec}}$. Thus, it is calculated from the polar decomposition of the deformation gradient $\boldsymbol{F}$ that corresponds to the displacements $\boldsymbol{u}_i$ of the nodes within the element. Finally, $\boldsymbol{F}_{\mathrm{tec}}$ can be calculated using Eq. 7, and subsequently the viscous stress $\boldsymbol{\sigma}_{\mathrm{visc}}$ can be obtained from Eq. 5 and Eq. 6 with $\boldsymbol{F} = \boldsymbol{F}_{\mathrm{tec}}$.

To account for rate-dependent material behavior within the solid-shell element, Eqs. 3 to 8 are applied separately as constitutive equations for the membrane and the bending behavior. In summary, Eq. 2 reads

$$\boldsymbol{S} = \underbrace{\boldsymbol{S}^*_{\mathrm{M}}\left(\boldsymbol{E}_{\mathrm{M}}, \dot{\boldsymbol{E}}_{\mathrm{M}}\right) + \boldsymbol{S}^*_{\mathrm{B}}\left(\boldsymbol{E}_{\mathrm{B}}, \dot{\boldsymbol{E}}_{\mathrm{B}}\right)}_{\boldsymbol{S}^*} + \boldsymbol{S}^{\mathrm{hg}}\left(\boldsymbol{E}^{\mathrm{hg}}_{\mathrm{c}}\right) \tag{9}$$

for the considered viscoelastic material law. Note that the hourglass stabilization is modeled purely elastic and thus can be adopted from Schäfer et al. [13].

Estimation of timestep increment. The implementation in ABAQUS/EXPLICIT requires the definition of an approximation for the upper bound of the stable time increment Δt. Using the stability limit Δt_{c} obtained from Courant, Friedrichs and Lewy [27] and the safety factor $\alpha \in (0,1]$ the upper bound for Δt is obtained by

$$\Delta t = \alpha \Delta t_{\mathrm{c}} \leq \alpha \frac{L_{\mathrm{e}}}{c_{\mathrm{d}}}, \tag{10}$$

where L_{e} remarks the smallest geometric element dimension and c_{d} the dilatational wave speed. The dilatational wave speed c_{d} is dependent on the material law. Since solid-shell elements are thin structures, L_{e} and subsequently Δt_{c} are very small. For an isotropic elastic material law c_{d} can be computed using [28]

$$c_{\mathrm{d}} = \sqrt{\frac{\lambda + 2\mu}{\rho}}, \tag{11}$$

where λ and μ denote the Lamé constants and ρ the mass density of an isotropic linear elastic material. However, in this work a viscoelastic material law is considered which is described by the Voigt-Kelvin model in Eq. 3. As this material is rate-dependent, it is not appropriate to assume that the corresponding dilatational wave speed c_{d} from Eq. 11 is constant. Thus, it is possible that the calculated upper bound Δt for the stable timestep is estimated too large which leads to unstable iteration schemes. Hence, it is beneficial to calculate an effective dilatational wave speed $\hat{c}_{\mathrm{d}}$ which is dependent on resulting stresses $\boldsymbol{S}$ and strains $\boldsymbol{E}$. This enables the calculation of a stable time increment Δt for arbitrary material laws. To calculate an effective dilatational wave speed $\hat{c}_{\mathrm{d}}$, the compression modulus $\widehat{K}$ and shear modulus $\hat{\mu}$ for an effective isotropic linear elastic material are calculated using the hyperelastic St. Venant-Kirchhoff model [24]

$$3\widehat{K}(\boldsymbol{E}^{\circ} \cdot \boldsymbol{E}^{\circ}) = \boldsymbol{S}^{\circ} \cdot \boldsymbol{E}^{\circ} \text{ and } 2\hat{\mu}(\boldsymbol{E}' \cdot \boldsymbol{E}') = \boldsymbol{S}' \cdot \boldsymbol{E}'. \tag{12}$$

The operators $(\cdot)^{\circ}$ and $(\cdot)'$ denote the spherical and deviatoric parts of second-order tensors. Finally, the effective Lamé constants $\hat{\lambda}$ and $\hat{\mu}$ can be obtained from $\widehat{K}$ and $\hat{\mu}$ in Eq. 12 and subsequently be substituted into Eq. 11 to calculate the effective dilatational wave speed $\hat{c}_{\mathrm{d}}$. To calculate the effective dilatational wave speed $\hat{c}_{\mathrm{d}}$ for the solid-shell element, the stress $\boldsymbol{S}^{*} = \boldsymbol{S}^{*}_{\mathrm{M}} + \boldsymbol{S}^{*}_{\mathrm{B}}$ and the Green-Lagrange strain $\boldsymbol{E}^{*} = \boldsymbol{E}_{\mathrm{M}} + \boldsymbol{E}_{\mathrm{B}}$ are used.
Note, that no effective material constants $\widehat{K}$ and $\hat{\mu}$ can be estimated from Eq. 12 if e.g., $\boldsymbol{E}^{*} = \boldsymbol{0}$. Hence, the provided time step estimation is applied only when the estimated time step using Eq. 12 is smaller than the time step derived from the purely elastic case. Otherwise, the estimated time step from the purely elastic case is applied.

Numerical Study

To demonstrate the rate-dependent material law based on Eq. 9, the solid-shell element is loaded with simple tensile tests and cantilever-bending tests. In both tests the beam has the length $l = 30$ mm, the width $b = 5$ mm and the thickness $t = 0.3$ mm. In total, six elements are used to discretize the beam with only one element layer in thickness-direction $\boldsymbol{e}_3$. The geometry of the beam and the load cases are displayed in Fig. 1. The beams for both load cases are fixed on the left-hand side while the load is applied on the tip of the beam. The tensile test (Fig. 1a) is performed displacement-controlled. The maximum tension applied in the tensile test (Fig. 1a) is $u_{\mathrm{M,max}} = 10$ mm. The cantilever-bending test (Fig. 1b) is performed load-controlled. The maximum load applied in the cantilever-bending test (Fig. 1b) is $F_{\mathrm{B,max}} = 2.5$ mN. A smoothed amplitude is used to ramp-up the load-amplitude from zero to the maximum value for both coupon-tests.

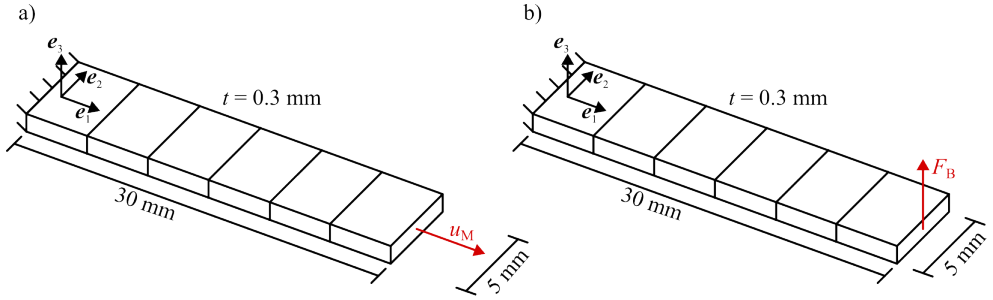

Figure 1: Geometries and load cases for the tensile test (a) and the cantilever test (b).

Since this work focuses on the rate-dependent (viscous) part of the implemented material law, the elastic part of the material law (Eq. 4) is kept constant and equal for both the membrane and bending behavior throughout this work. It is described by the anisotropic stiffness tensor in Voigt notation

$$\mathbb{C}_{\mathrm{M}} = \mathbb{C}_{\mathrm{B}} = \begin{bmatrix} 100 & 0 & 0 & 0 & 0 & 0 \\ 0 & 10 & 0 & 0 & 0 & 0 \\ 0 & 0 & 10 & 0 & 0 & 0 \\ 0 & 0 & 0 & 10 & 0 & 0 \\ 0 & 0 & 0 & 0 & 10 & 0 \\ 0 & 0 & 0 & 0 & 0 & 10 \end{bmatrix} \boldsymbol{V}_{\xi} \otimes \boldsymbol{V}_{\eta} \text{ MPa}. \tag{12}$$

where $\boldsymbol{V}_{\xi}$ denote the basis dyads of the Voigt notation.

Membrane-bending decoupling. To demonstrate that the membrane-bending decoupling still holds for the viscoelastic material law, simple tensile and cantilever tests are performed. For the elastic part, Schäfer et al. [13] showed that a membrane-bending decoupling is considered correctly with the presented solid-shell element. In the present work a similar approach is considered to demonstrate the membrane-bending decoupling for the viscous part of the viscoelastic material

law (Eq. 5). Virtual tensile and cantilever tests (Fig. 1) are performed with a constant velocity. The viscosities η_{M} and η_{B} (cf. Eq. 5) for the membrane and bending behavior, respectively, are both varied between a low viscosity $\eta^{\mathrm{low}} = 0.1\ \mathrm{MPa} \cdot \mathrm{s}$ and a high viscosity $\eta^{\mathrm{high}} = 1\ \mathrm{MPa} \cdot \mathrm{s}$.

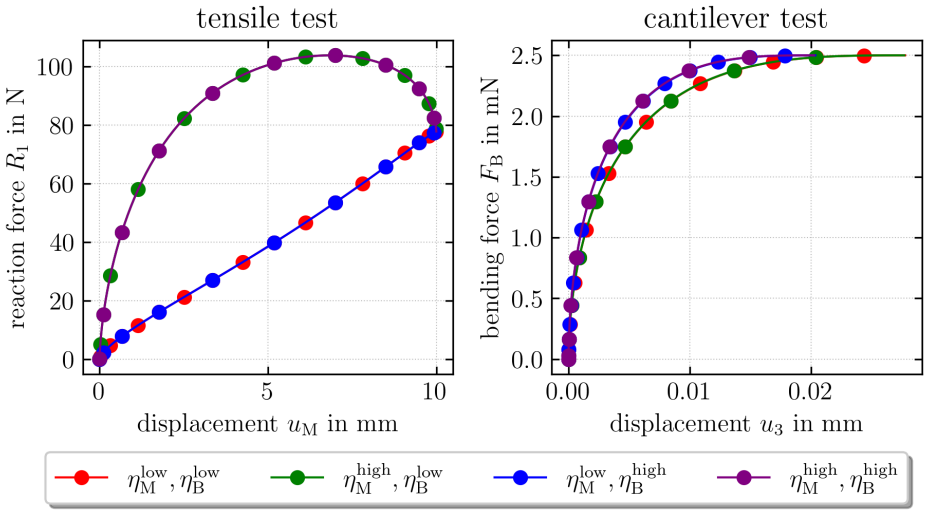

Figure 2: Resulting virtual material response for different combinations of high and low viscosities for both the membrane and the bending behavior.

The results for both the tensile tests and the cantilever tests are depicted in Fig. 2. The different combinations of high and low viscosities for the membrane and bending behavior are symbolized using different colors. Since the trajectories partially overlap, colored dots are used to distinguish the different curves. The results of the tensile test in Fig. 2 indicate that the reaction force in deformation direction undergoes changes solely when there is a variation in membrane viscosity η_{M}. A change of the bending viscosity η_{B} does not affect the result of the tensile test. Analogously, the cantilever bending tests in Fig. 2 shows that the resulting trajectory is only dependent on the bending viscosity η_{B} and a change of the membrane viscosity η_{M} does not affect the result of the cantilever-bending test. In summary it can be concluded that the membrane-bending decoupling still holds for the viscous material behavior.

Demonstration of the rate-dependent membrane behavior. To investigate the rate-dependency of the viscoelastic material law inside the membrane behavior, displacement-controlled tensile tests (Fig. 1a) are performed. The membrane viscosity is chosen equally for all tensile tests $\eta_{\mathrm{M}} = 1\ \mathrm{MPa} \cdot \mathrm{s}$. The bending viscosity is omitted for the tensile tests since the above results (cf. Fig. 2) indicated that the bending viscosity η_{B} does not affect the result of the tensile test. The results of the viscoelastic tensile tests are compared with the purely elastic case where the viscous part of the membrane behavior is neglected ($\eta_{\mathrm{M}} = 0\ \mathrm{MPa} \cdot \mathrm{s}$).

The results of the tensile tests are displayed in Fig. 3. Here, the evolution of the reaction force R_1 in load direction are displayed over the displacement u_{M} in load direction. The different colors represent different load times respectively load rates. The blue line represents the elastic case which is time independent. In the elastic case, the reaction force R_1 increases monotonically with increasing displacement u_{M}. Due to the geometric nonlinearity of the strain $\boldsymbol{E}$, the trajectory of R_1 is not linear over u_{M}. In case of the viscoelastic material law, the reaction force R_1 increases with increasing deformation speed for a certain displacement u_{M}. This is due to the larger deformation rate tensor $\boldsymbol{D}$ for larger deformation rates. This shows that the general concept of viscoelasticity is captured accurately, and a rate-dependent material law can be displayed using the viscoelastic solid-shell element. The viscous curves do not follow a monotonic pattern. However, they approach the same reaction force R_1 as observed in the elastic case. This is due to the smoothed load amplitude which starts and ends with very small deformation rates. Since the deformation

Materials Research Proceedings 41 (2024) 457-466 https://doi.org/10.21741/9781644903131-51

rate tensor $\boldsymbol{D}$ nearly vanishes for $u_{\mathrm{M}} \approx u_{\mathrm{M,max}}$ the resulting reaction force is only caused by the elastic contribution of the material law. Therefore, it can be inferred that the variation in force between the elastic curve (blue) and the viscoelastic curves (red, green, orange) is solely attributed to viscoelastic properties.

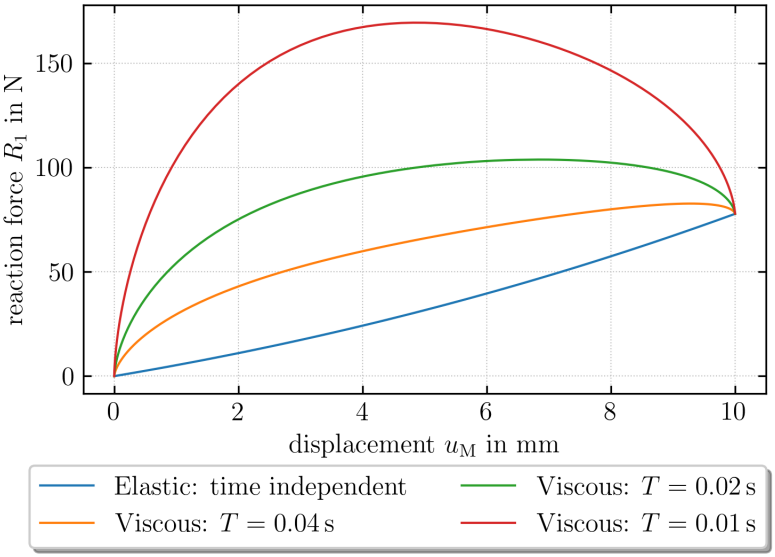

Figure 3: Resulting reaction forces for different deformation rates for the membrane behavior of the viscoelastic solid-shell element.

Demonstration of the rate-dependent bending behavior. To investigate the rate-dependency of the viscoelastic material law of the bending behavior the cantilever-bending test is performed force-controlled (Fig. 1b). The bending viscosity is chosen equally for all cantilever-bending tests $\eta_{\mathrm{B}} = 1\ \mathrm{MPa}\ \cdot \mathrm{s}$. The membrane viscosity is omitted for the bending tests since Fig. 2 showed that the membrane viscosity η_{M} does not affect the result of the cantilever-bending test. The results of the viscoelastic cantilever-bending tests are compared with the purely elastic case. Here the viscous part of the bending behavior is also neglected ($\eta_{\mathrm{B}} = 0\ \mathrm{MPa}\ \cdot \mathrm{s}$).

The results of the different cantilever-tests are displayed in Fig. 4. Here, the curves of the applied bending force F_{B} over the resulting displacement of the tip of the beam u_3 are displayed. The different colors represent different load times respectively load speeds. The blue line represents the elastic case which is time independent. For elastic material behavior, the flattest curve is attained. Furthermore, an increase in load speed corresponds to a steeper trajectory of the bending force F_{B} for the deformation u_3. Conversely, an increased load speed demands more bending force F_{B} for the same tip displacement u_3. This is attributed to a greater deformation rate tensor $\boldsymbol{D}$ for higher load speeds. Consequently, it can be deduced that the material's rate-dependent behavior can be captured under bending load.

Note that none of the simulations in Fig. 4 reach a stationary state and all trajectories become nearly horizontal towards the end of the simulation time. For the viscous simulations (red, green, orange), the condition $\boldsymbol{D} \approx \boldsymbol{0}$ does not hold immediately at $F_{\mathrm{B}} = F_{\mathrm{B,max}}$ because the bending test is performed force-controlled (Fig. 1b). Thus, the elastic equilibrium, where all trajectories meet in the same point, is only reached for large simulation times. Since the major rate-dependent effects of the viscoelastic bending behavior are observable using the initial slope of the trajectories, larger simulation times are not considered in this work.

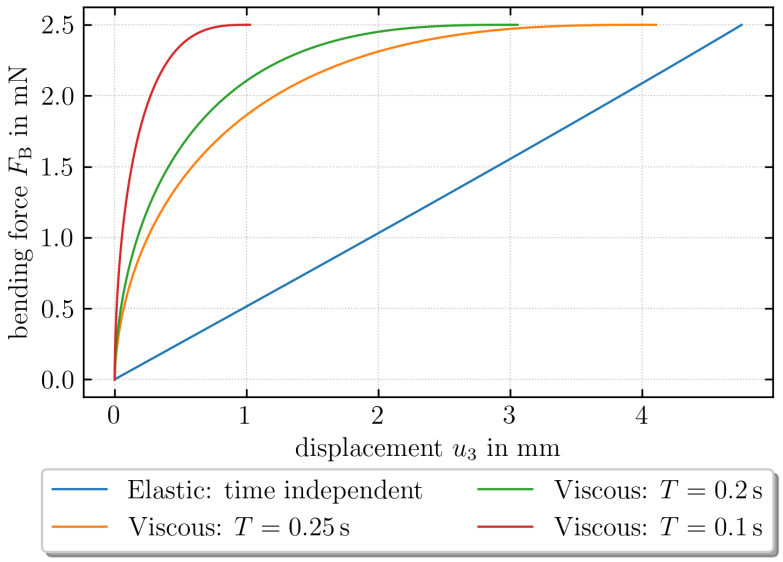

Figure 4: Resulting displacements for different load rates for the bending behavior of the viscoelastic solid-shell element.

Conclusion and outlook

This work presents the enhancement of a locking-free linear elastic and anisotropic solid-shell element to a viscoelastic solid-shell element for a future application in thermoforming simulation of thermoplastic tapes. The considered solid-shell element is implemented as a user-element (VUEL) in ABAQUS/EXPLICIT. The Voigt-Kelvin model is used to model both the membrane and the bending behavior of the solid-shell element. It is shown that the presented approach can preserve the membrane-bending decoupling for the viscous stresses in coupon-tests. Thus, the viscoelastic material law can be applied to both the membrane and the bending behavior independently. An alternative estimation of the stable time-increment is presented which takes viscoelastic stresses into account. Numerical studies are carried out to demonstrate the viscoelastic material law in coupon-tests. The results show that the rate-dependent material behavior is working for both the membrane and the bending-part of the solid-shell element. Thus, the general approach of the viscoelastic material behavior within the solid-shell element is suitable as a further step addressing out-of-plane phenomena in thermoforming simulations with a solid-shell element.

In this study only generic material properties were used to test the rate-dependent material laws. Future studies will extend the presented viscoelastic approach to more realistic material behavior to model the forming behavior of preimpregnated textile composites. A comparison of results of the conventional shell-elements and the solid-shell elements will be carried out to investigate the advantages of constitutive modeling the out-of-plane forming behavior.

Acknowledgements

This work has been carried out in the DFG AI Research Unit 5339, funded by the Deutsche Forschungsgemeinschaft (DFG, German Research Foundation) – 459291153. The work is also part of the Heisenberg project ‘Digitalization of fiber-reinforced polymer processes for resource-efficient manufacturing of lightweight components’, funded by the DFG (project no. 798455807141). The authors thank the German Research Foundation for its financial support.

References

[1] F. Henning, L. Kärger, D. Dörr, F.J. Schirmaier, J. Seuffert, A. Bernath, Fast processing and continuous simulation of automotive structural composite components, Composites Science and Technology 171 (2019) 261–279. https://doi.org/10.1016/j.compscitech.2018.12.007

[2] P. Bussetta, N. Correia, Numerical forming of continuous fibre reinforced composite material: A review, Composites Part A: Applied Science and Manufacturing 113 (2018) 12–31. https://doi.org/10.1016/j.compositesa.2018.07.010

[3] B. Schäfer, D. Dörr, L. Kärger, Reduced-Integrated 8-Node Hexahedral Solid-Shell Element for the Macroscopic Forming Simulation of Continuous Fibre-Reinforced Polymers, Procedia Manufacturing 47 (2020) 134–139. https://doi.org/10.1016/j.promfg.2020.04.154

[4] U. Sachs, R. Akkerman, Viscoelastic bending model for continuous fiber-reinforced thermoplastic composites in melt, Composites Part A: Applied Science and Manufacturing. https://doi.org/10.1016/j.compositesa.2017.05.032

[5] A. Margossian, S. Bel, R. Hinterhoelzl, Bending characterisation of a molten unidirectional carbon fibre reinforced thermoplastic composite using a Dynamic Mechanical Analysis system, Composites Part A: Applied Science and Manufacturing 77 (2015) 154–163. https://doi.org/10.1016/j.compositesa.2015.06.015

[6] S. Ropers, M. Kardos, T.A. Osswald, A thermo-viscoelastic approach for the characterization and modeling of the bending behavior of thermoplastic composites, Composites Part A: Applied Science and Manufacturing 90 (2016) 22–32. https://doi.org/10.1016/j.compositesa.2016.06.016

[7] D. Dörr, F. Henning, L. Kärger, Nonlinear hyperviscoelastic modelling of intra-ply deformation behaviour in Finite element forming simulation of continuously fibre-reinforced thermoplastics, Composites Part A: Applied Science and Manufacturing. https://doi.org/10.1016/j.compositesa.2018.03.037

[8] D. Dörr, F.J. Schirmaier, F. Henning, L. Kärger, A viscoelastic approach for modeling bending behavior in finite element forming simulation of continuously fiber reinforced composites, Composites Part A: Applied Science and Manufacturing 94 (2017) 113–123. https://doi.org/10.1016/j.compositesa.2016.11.027

[9] D. Dörr, T. Joppich, D. Kugele, F. Henning, L. Kärger, A coupled thermomechanical approach for finite element forming simulation of continuously fiber-reinforced semi-crystalline thermoplastics, Composites Part A: Applied Science and Manufacturing 125 (2019). https://doi.org/10.1016/j.compositesa.2019.105508

[10] Hu Xiong, Simulation of forming, compaction and consolidation of thermoplastic composites based on solid shell elements, 2018.

[11] H. Xiong, N. Hamila, P. Boisse, Consolidation Modeling during Thermoforming of Thermoplastic Composite Prepregs, Materials (Basel, Switzerland) 12 (2019). https://doi.org/10.3390/ma12182853

[12] P.D. Mulye, L. Morançay, C. Binetruy, S. Comas-Cardona, A. Leygue, D. Guillon, Unified numerical process modeling of forming and consolidation for thermoplastic composites with prepreg patches, Front. Mater. 10 (2023). https://doi.org/10.3389/fmats.2023.1176482

[13] B. Schäfer, D. Dörr, L. Kärger, Potential and challenges of a solid-shell element for the macroscopic forming simulation of engineering textiles, ESAFORM 2021. https://doi.org/10.25518/esaform21.883

[14] M. Schwarze, S. Reese, A reduced integration solid-shell finite element based on the EAS and the ANS concept-Geometrically linear problems, Int. J. Numer. Meth. Engng. 80 (2009) 1322–1355. https://doi.org/10.1002/nme.2653

[15] M. Schwarze, S. Reese, A reduced integration solid-shell finite element based on the EAS and the ANS concept-Large deformation problems, Int. J. Numer. Meth. Engng. 85 (2011) 289–329. https://doi.org/10.1002/nme.2966

[16] M. Pagani, S. Reese, U. Perego, Computationally efficient explicit nonlinear analyses using reduced integration-based solid-shell finite elements, Computer Methods In Applied Mechanics And Engineering 268 (2014) 141–159. https://doi.org/10.1016/j.cma.2013.09.005

[17] K. Jože, Multi-language and Multi-environment Generation of Nonlinear Finite Element Codes, Engineering with Computers 18 (2002) 312–327. https://doi.org/10.1007/s003660200028

[18] J.C. Simo, M.S. Rifai, A class of mixed assumed strain methods and the method of incompatible modes, Int. J. Numer. Meth. Engng. 29 (1990) 1595–1638. https://doi.org/10.1002/nme.1620290802

[19] J.C. Simo, F. Armero, Geometrically non-linear enhanced strain mixed methods and the method of incompatible modes, Int. J. Numer. Meth. Engng. 33 (1992) 1413–1449. https://doi.org/10.1002/nme.1620330705

[20] J. Simo, F. Armero, R. Taylor, Improved versions of assumed enhanced strain tri-linear elements for 3D finite deformation problems, Computer Methods In Applied Mechanics And Engineering 110 (1993) 359–386.

[21] T.J.R. Hughes, T.E. Tezduyar, Finite Elements Based Upon Mindlin Plate Theory With Particular Reference to the Four-Node Bilinear Isoparametric Element, J. Appl. Mech 48 (1981) 587–596. https://doi.org/10.1115/1.3157679

[22] M. Schwarze, I.N. Vladimirov, S. Reese, On the implementation of the EAS and ANS concept into a reduced integration continuum shell element and applications to sheet forming, Int J Mater Form 2 (2009) 919–922. https://doi.org/10.1007/s12289-009-0634-2.

[23] A. Bertram, Elasticity and Plasticity of Large Deformations, Springer International Publishing, Cham, 2021.

[24] T. Belytschko, W.K. Liu, B. Moran, K.I. Elkhodary, Nonlinear finite elements for continua and structures, 2nd ed., Wiley, Chichester, 2014.

[25] C.W. Macosko, Rheology: Principles, measurements, and applications, Wiley-VCH, New York NY u.a., 1994.

[26] R. Hauptmann, K. Schweizerhof, S. Doll, Extension of the 'solid-shell' concept for application to large elastic and large elastoplastic deformations, Int. J. Numer. Meth. Engng. 49 (2000) 1121–1141. https://doi.org/10.1002/1097-0207(20001130)49:9<1121:AID-NME130>3.0.CO;2-F

[27] R. Courant, K. Friedrichs, H. Lewy, Über die partiellen Differenzengleichungen der mathematischen Physik, Math. Ann. 100 (1928) 32–74. https://doi.org/10.1007/BF01448839

[28] G. Cocchetti, M. Pagani, U. Perego, Selective mass scaling and critical time-step estimate for explicit dynamics analyses with solid-shell elements, Computers & Structures 127 (2013) 39–52. https://doi.org/10.1016/j.compstruc.2012.10.021